PNAS
www.pnas.org

Supplementary Information for

A structural and dynamical rationale for fatty acid unsaturation in *E. coli*

Greg J. Dodge[+], Ashay Patel[+], Kara L. Jaremko[+], J. Andrew McCammon*, Janet L. Smith*, and Michael D. Burkart*

Michael D. Burkart
Email: mburkart@ucsd.edu

Janet L. Smith
Email: JanetSmith@umich.edu

J. Andrew McCammon
Email: mccammon@ucsd.edu

This PDF file includes:

Supplementary text
Figs. S1 to S22
Tables S1 to S4
References for SI reference citations

www.pnas.org/cgi/doi/10.1073/pnas.1818686116

A. Chemical and Biological Protocols

B. Molecular Dynamic Simulation Protocols

C. Supplementary Figures and Tables

D. Additional References

A. Chemical and Biological Protocols

A.1. *Cloning and Gene Expression*

***fabZ*:** Previous reports indicated *E. coli* FabZ was soluble when expressed recombinantly with a C-terminal His tag. (1) As reported by others, we found that recombinant FabZ was neither stable nor monodisperse when purified, so an optimized construct encoding a TEV-protease-cleavable N-terminal Mocr fusion protein and residues 2-150 of *E. coli* FabZ was cloned into the pMocr expression vector to create pGJD026 (Table S4). (2) *E. coli* strain BL21-AI (Thermo Fisher) was co-transformed with pGJD026 and pRARE2-CDF. (3) A 0.5 L culture in 4% glycerol Terrific Broth media (BD) with 100 mg/L ampicillin and 50 mg/L spectinomycin was grown at 37°C to an optical density at 600 nm (OD_{600}) of 1.5, cooled to 20°C, induced by the addition of isopropyl β-D-1-thiogalactopyranoside (IPTG) to 0.2 mM and 1 g solid (L)-arabinose, and incubated 18 hr. Cells were harvested via centrifugation. Cell pellets were transferred to 50 mL Falcon tubes, immediately frozen and stored at -20°C.

***acpP*:** *E. coli acpP* was cloned into the pMCSG7 expression vector to create pGJD042. (4) *E. coli* strain BL21-AI (Thermo Fisher) was co-transformed with pGJD042 and pRARE2-CDF. (3) A 0.5 L culture in 4% glycerol Terrific Broth media (BD) with 100 mg/L ampicillin and 50 mg/L spectinomycin was grown at 37°C to an OD_{600} of 1.5, cooled to 20°C, induced by the addition of isopropyl β-D-1-thiogalactopyranoside (IPTG) to 0.2 mM and 1 g solid (L)-arabinose, and incubated 18 hr. Cells were harvested via centrifugation. Cell pellets were transferred to 50 mL Falcon tubes, immediately frozen and stored at -20°C.

The construction of all expression plasmids was confirmed by sequencing.

A.2. *Protein Purification*

FabZ: All steps were performed at 4°C. Cell pellets were resuspended in buffer A (50 mM Tris pH 7.5, 300 mM NaCl, 15 mM imidazole, 10% glycerol) with 2 mM $MgCl_2$, 0.5 mg/mL DNase I,

and 0.06 mg/mL lysozyme (4 mL per g cell pellet), incubated on ice for 1 hr, then sonicated. The lysate was cleared by centrifugation. The supernatant was passed through a 0.2 μm filter and loaded onto a 5 mL HisTrap column (GE Healthcare). The column was washed with 10 volumes buffer A, and protein was eluted with a linear gradient from 15 mM to 400 mM imidazole in buffer A. Peak fractions were pooled, concentrated, and loaded on a Superdex 16/60 S200 gel filtration column (GE Healthcare) pre-equilibrated with buffer B (25 mM Tris pH 7.5, 150 mM NaCl, 10% glycerol). FabZ eluted as a hexamer, with an apparent molecular weight of 200 kDa (calculated MW 201 kDa). Peak fractions were pooled and loaded onto a HiTrap Q column. The column washed with 10 volumes buffer B, and protein was eluted with a linear gradient from 150 mM to 1 M NaCl in buffer B. Peak fractions were pooled, concentrated, and loaded on a Superdex 16/60 S200 gel filtration column pre-equilibrated with buffer B. Peak fractions were pooled, concentrated to 15 mg/mL, flash cooled in liquid N_2, and stored at -80°C.

AcpP: The protocol was identical to that for FabZ through the first step of metal affinity separation. Peak fractions were pooled, concentrated, and loaded on a Superdex 16/60 S75 gel filtration column pre-equilibrated with buffer B. Peak fractions were pooled, concentrated to 15 mg/mL, flash cooled in liquid N_2, and stored at -80°C.

A.3. *One-Pot AcpP Modification and FabZ Crosslinking*

Apo-AcpP was prepared from a mixture of apo- and holo-AcpP according to a previously published protocol[2]. The one-pot loading reactions were performed as previously reported.[3] Briefly, the 1-mL reaction mix contained 8 mM ATP, 0.5 μM CoaA, 0.7 μM CoaD, 0.6 μM CoaE, 1.5 μM Sfp, 0.4 mM apo-AcpP, 500 μM DH6 probe in Buffer D (100 mM phosphate pH 7.6, 100 mM NaCl, 10% glycerol). The mixture was rotated 24 hr at 37 °C. The formation of *crypto*-AcpP was monitored by urea-PAGE gel and LCMS (ESI) analyses. The *crypto*-AcpP was purified by

size exclusion (Superdex S75) and concentrated using a 3-kDa ultra centrifugation filter (Amicon) and stored at -80° C until needed.

Crosslinking of His_6-tagged *crypto*-DH6-AcpP and Mocr-FabZ was carried out in a 1.5:1 molar ratio for SEC-MALS analysis. For production of AcpP=FabZ for crystallization and SDS-PAGE analysis, a 1.1:1 ratio of His_6-tagged *crypto*-DH6-AcpP and Mocr-FabZ was used. A 1-mL crosslinking reaction in buffer D contained 150 μM Mocr-FabZ, 225 or 165 μM *crypto*-DH6-AcpP, and 0.5 mg/mL TEV protease, and was rotated 8 hr at 37 °C. Formation of the crosslinked complex and TEV protease cleavage of the Mocr fusion partner were monitored by SDS-PAGE. Reaction mixtures were loaded directly onto a Superdex S200 gel filtration column equilibrated with Buffer B. Peak fractions were pooled, combined and concentrated to 10 mg/mL.

A.4. *Mocr-FabZ TEV Protease Cleavage Turbidity Assay*

50 μM Mocr-FabZ was incubated in buffer C with TEV protease to a final concentration of 3.75 mg/mL in the presence of *apo*-AcpP at a final concentration of 0, 25, 50, 150, 300 or 500 μM. Cleavage reaction mixtures were incubated at 25 °C for 1 hr and turbidity was determined as OD_{600}. Concentrations of Mocr-FabZ refer to the subunit. Experiments were performed in triplicate.

A.5. *Size Exclusion Chromatography with Multi-Angle Light Scattering (SEC-MALS)*

40 μM Mocr-FabZ was mixed with *apo*-AcpP to a final concentration of 200 (1:5), 400 (1:10) or 800 (1:20) μM. 40 μM Mocr-FabZ was mixed with *holo*-AcpP to a final concentration of 200 (1:5) or 400 (1:10) μM. 20 μM Mocr-FabZ was mixed with *holo*-AcpP to a final concentration of 200 (1:20) μM. All samples were incubated 1 hr at 25 °C. 50 μL of each sample was loaded onto a Showdex KW-804 column (Phenomenex) pre-equilibrated with buffer E (25 mM Tris pH 7.5, 100 mM NaCl) at a flow rate of 0.4 mL/min. The eluent was passed through both a DAWN HELEOS II multi-angle light scattering detector (Wyatt), and a T-rEX differential

refractive index detector (Wyatt) pre-configured with a β-amylase standard. Data were analyzed using the ASTRA software package (Wyatt). Concentrations of Mocr-FabZ refer to the subunit. Experiments were performed in duplicate.

A.6. *Crystallography Details*

The AcpP-FabZ complex was crystallized at 20°C by hanging drop vapor diffusion in a 1:1 mix of 9.5 mg/mL protein stock and reservoir solution (100 mM Bis-Tris pH 6.5, 200 mM $MgCl_2$, 19% PEG 3350). Crystals were harvested without additional cryoprotectant and flash-cooled in liquid N_2.

Data were collected at the Advanced Photon Source (APS, Argonne National Laboratory) on GM/CA beamline 23-ID-D. Crystals diffracted to 2.5 Å and were in orthorhombic space group $P2_12_12_1$ containing one AcpP=FabZ hexamer per asymmetric unit. Data were processed using XDS[4]. The AcpP-FabZ structure was solved by molecular replacement in phaser using the *P. aeuroginosa* FabZ as an initial search model (PDB: 1U1Z (5)). (6) Six AcpPs were placed manually into electron density using the AcpP from the AcpP=FabA structure (PDB: 4KEH (7)) in coot. (8) The resulting atomic model was refined in PHENIX (Table S2). (9) The refined model was validated with MolProbity. (10) Structure figures were generated in PyMOL. (11) Protein-protein interfaces were calculated using the PISA server. (12)

The atomic coordinates and structure factors for the AcpP=FabZ complex have been deposited in the RCSB Protein Data Bank under the accession code 6N3P.

B. Molecular Dynamic Simulation Protocols

B1. Simulation Preparation

Initial coordinates were prepared using the previously reported crystal structure of crosslinked AcpP=FabA (6) and a 3.4 Å AcpP=FabZ structure. Simulations were performed before

the higher resolution (2.5 Å) AcpP=FabZ structure described in the main text was solved. The two AcpP=FabZ structures differed in RMS deviation by 0.641 Å (computed over all Cα of the crosslinked complex). Note that while the AcpP•FabZ is hexameric, a DH dimer was simulated for reasons of computational tractability. The phosphopantetheinylated serine bearing the acyl substrates (or product) in each system was treated as a nonstandard residue. Partial atomic charges for these nonstandard residues were determined using the restrained electrostatic potential (RESP) methodology. (12) The potential was computed at the HF/6-31G(d) level of theory using Gaussian 09. AMBER (ff14SB) and GAFF type parameters were assigned to the atoms of these residues using ANTECHAMBER. (13-15) The protonation states of all systems were determined using the H++ webserver, (16-19) assuming an external dielectric constant of 80, salinity of 150 mM, and at pH 7.4. The protonation states of all histidine residues were manually confirmed. All acyl-ACP•DH complexes were solvated with a TIP3P water box large enough that no proteinogenic atom was within 12 Å of the box edge. (20) Na^+ and Cl^- were added to the system to neutralize the anionic complex and to mimic the salt content of physiological systems (ca. 150 mM). TLEAP was used to solvate and add counterions to these systems. (21)

B2. Simulation Details

Gaussian accelerated molecular dynamics (GaMD) simulations were performed using Amber14. (22-26) The ff14SB[19] force field was employed in all simulation work. The SHAKE algorithm was used to constrain all nonpolar bonds involving hydrogen atoms and all TIP3P water molecules, (27) and a 2-fs time-step was used in the simulations. The Particle Mesh Ewald (PME) method was used to treat long-range electrostatic interactions using a 10.0 Å cutoff for nonbonded interactions. (28) Before simulations of the complexes were performed, all systems were subjected to a two-step minimization. In the first step, the solvent was allowed to relax, while the atoms in the solute were restraint using a harmonic potential (500 kcal mol^{-1} A^{-2}). Subsequently, the entire

system was minimized without constraints. After minimization, each system was slowly heated to 305 K over the course of a 3.5 ns canonical ensemble (NVT) MD simulation. These "heated" systems were subsequently equilibrated for 6 ns by performing unbiased isobaric-isothermal (NPT) simulations (at 305 K). In all simulations, temperature control was maintained using a Langevin thermostat (λ = 1.0 ps^{-1}). (29) For all NPT simulations, a Monte Carlo barostat was used.

Three independent 290 ns production-grade NPT GaMD simulations were performed for each acyl-AcpP•DH complex. The threshold energy was set to V_{max}. A 16 ns unbiased NPT simulation was used collect data to determine the maximum (V_{max}), minimum (V_{min}), average (V_{av}), and the standard deviation (σ_v) of the system potential. These data were not used in our analysis.

B3. Data Analysis and Molecular Visualization

Coordinate data were written to disk every 0.5 ps. Analysis was performed using PYTRAJ, a Python-based front-end for the CPPTRAJ software package, and MDTRAJ. Gaussview 5, Avogadro, and PyMol v1.8.6 were used to prepare and visualize structures. (10, 30-33) PyMol was used to render the images shown herein.

B4. POcket Volume Measurer Analysis

Pocket Volume Measurer 3.0 (POVME) analysis(34-36) was performed to characterized the volumes and shapes of the substrate binding cavities of FabA and FabZ sampled during the course of MD simulations. Analysis was performed on a subset of the complete coordinate data; every 4000^{th} simulation frame was subjected to POVME analysis. Simulation frames for each complex were pre-aligned (C_α) using the first frame of each trajectory as reference. In all cases, cluster analysis using a script available in POVME 3.0 was performed to identify a representative ("average") cavity volume for each complex simulated. Cluster analysis was performed by

generating a Tanimoto matrix, which was then used to perform hierarchal clustering. These cavities are shown in Figure 8 and SI Appendix, Figures S19-S22.

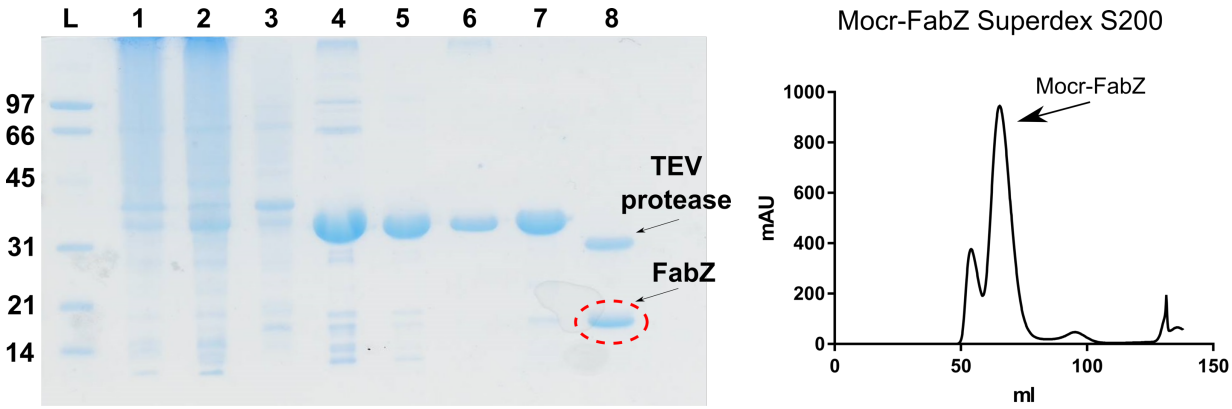

Figure S1. FabZ purification and solubilization. *Left*: SDS PAGE, Lane 1: Total lysate from production of recombinant Mocr-FabZ; Lane 2: Soluble fraction; Lane 3: Insoluble fraction; Lane 4: HisTrap elution; Lane 5: Superdex S200 #1; Lane 6: Ion exchange; Lane 7: Superdex S200 #2; Lane 8: Resolubilized precipitated protein following TEV protease treatment. *Right*: Elution profile from Superdex S200 gel filtration run (lane 7). Mocr-FabZ elutes as a hexamer with an apparent molecular weight of 201 kDa.

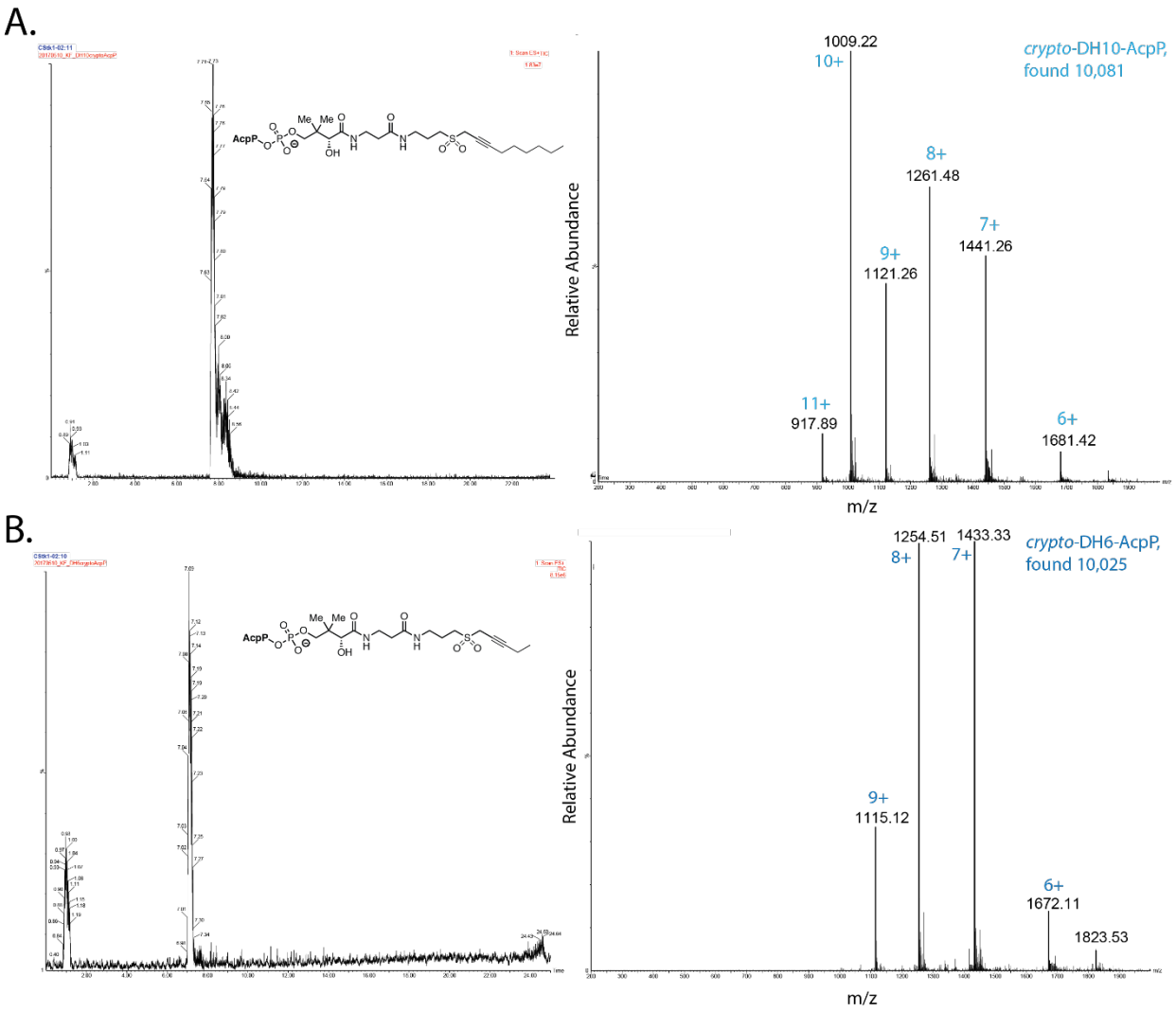

Figure S2. *Crypto*-DH6-AcpP and *crypto*-DH10-AcpP analysis. Previously synthesized DH6 and DH10 probes[14] were loaded onto AcpP using "one-pot" methods, and the *crypto*-AcpPs purified by size exclusion chromatography and analyzed by HPLC-MS (ESI) in positive mode and the charge distribution deconvoluted. (*A*) *Crypto*-DH10-AcpP analysis, showing LC trace (left) and mass analysis of the t=7.33 min protein peak (right, m/z). (*B*) *Crypto*-DH6-AcpP analysis, showing LC trace (left) and mass analysis of the t=7.09 min protein peak (right, m/z).

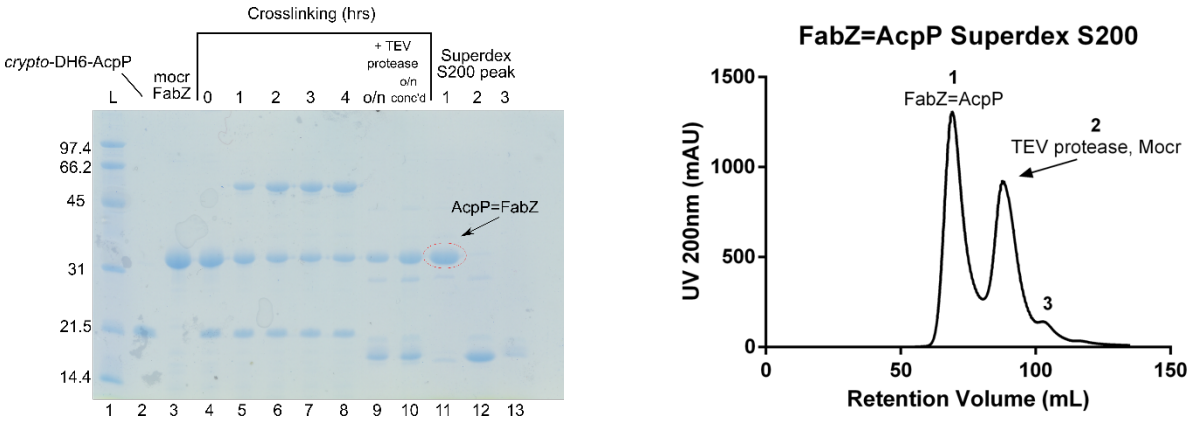

Figure S3. AcpP=FabZ purification and analysis. *Left***:** SDS PAGE, Lane 1: Ladder, Lane 2: *crypto*-DH6-AcpP; Lane 3: Mocr-FabZ; Lanes 4-8: crosslinking reaction mixture (*crypto*-DH6-AcpP:Mocr-FabZ in a 1.5:1 molar ratio) at several time points; Lane 9: Overnight crosslinking reaction in the presence of TEV protease; Lane 10: Overnight crosslinking reaction in the presence of TEV protease after concentrating with a 100K Amicon filter (Millipore); Lanes 11-13: Peak fractions of the gel filtration profile shown at right. FabZ=AcpP remained soluble following gel filtration. Mocr and TEV were readily separated from AcpP=FabZ via size exclusion chromatography. *Right***:** Superdex S200 gel filtration profile of crosslinking reaction mix in the presence of TEV protease. FabZ=AcpP (peak 1, lane 10 in the gel at left) was readily separated from the other components and used for crystallization. The FabZ=AcpP peak height exhibits low signal at 280 nm due to the low molar absorptivity of the both FabZ (calculated ε = 3,105) and AcpP (calculated ε = 1,490), compared to Mocr (calculated ε = 18,910) and TEV protease (calculated ε = 33,585). FabZ=AcpP elutes as a hexamer with an apparent molecular weight of 160 kDa.

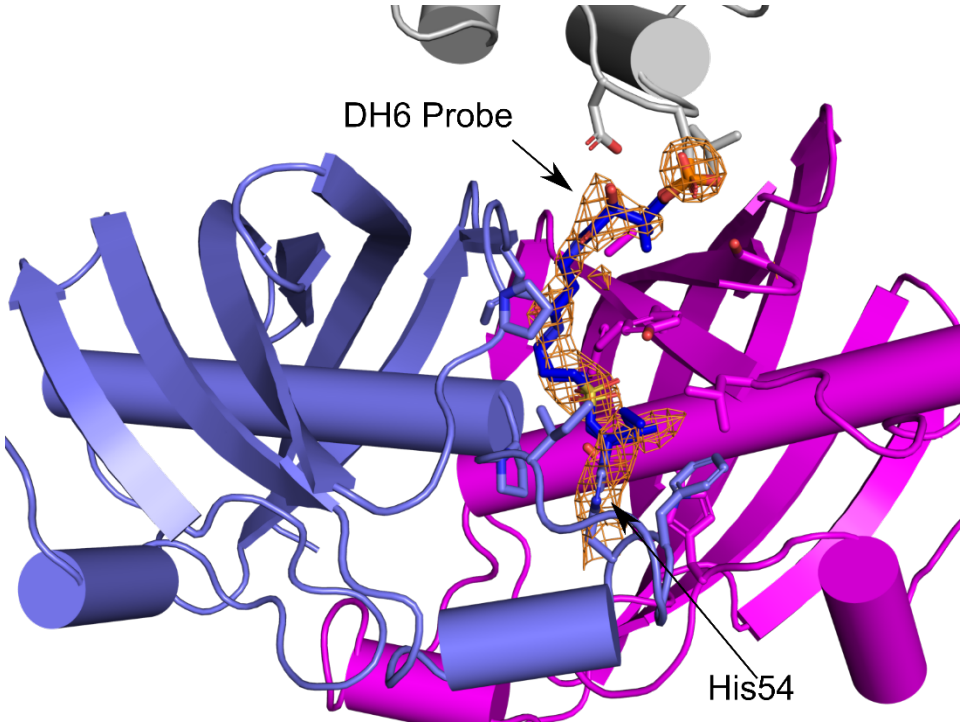

Figure S4. Electron density for the DH6 probe crosslinked to His54. Amino acid side chains within 5 Å of the DH6 probe are shown as sticks. Electron density (simulated annealing omit density contoured to 3σ) is shown in orange mesh. Continuous density is observed for the DH6 probe.

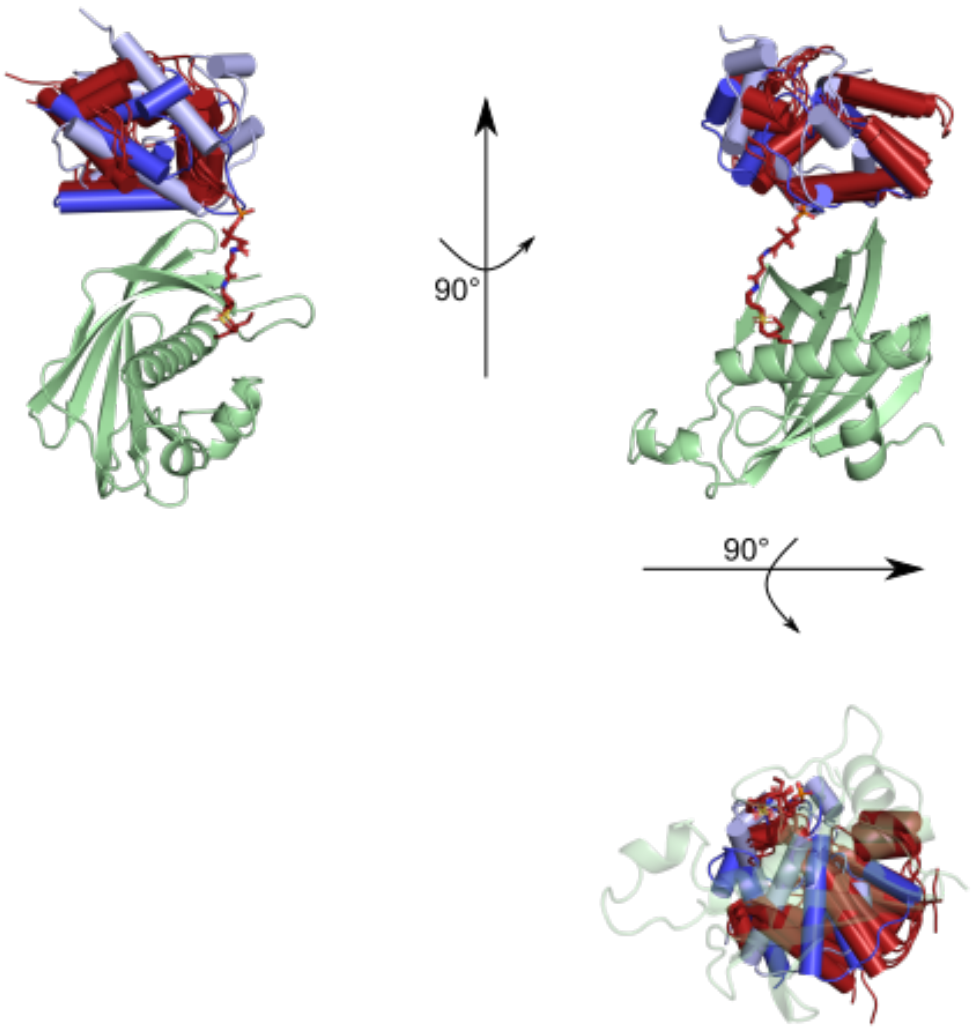

Figure S5. Position of crosslinked AcpP relative to the non-crosslinked DH monomer. Shown in red, four of the six crosslinked AcpPs occupy similar positions. Shown in light and dark blue, the two remaining AcpPs are shifted due to crystal packing. Non-crosslinked DH monomer shown in light green. DH6 crosslinker shown in stick form with atomic colors (red C atoms).

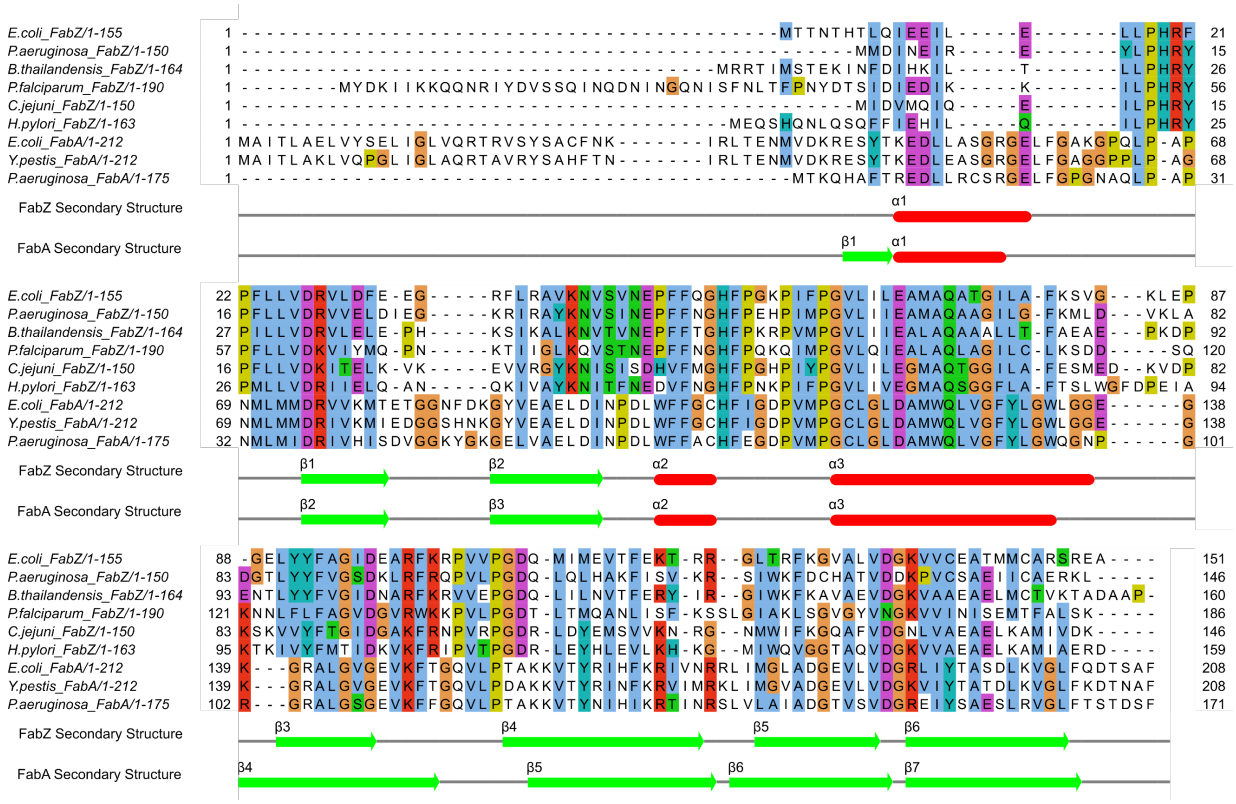

Figure S6. Sequence alignment of FabZ and FabA from select biological sources. α-helical secondary structure denoted as red tubes, β-strands denoted by green arrows.

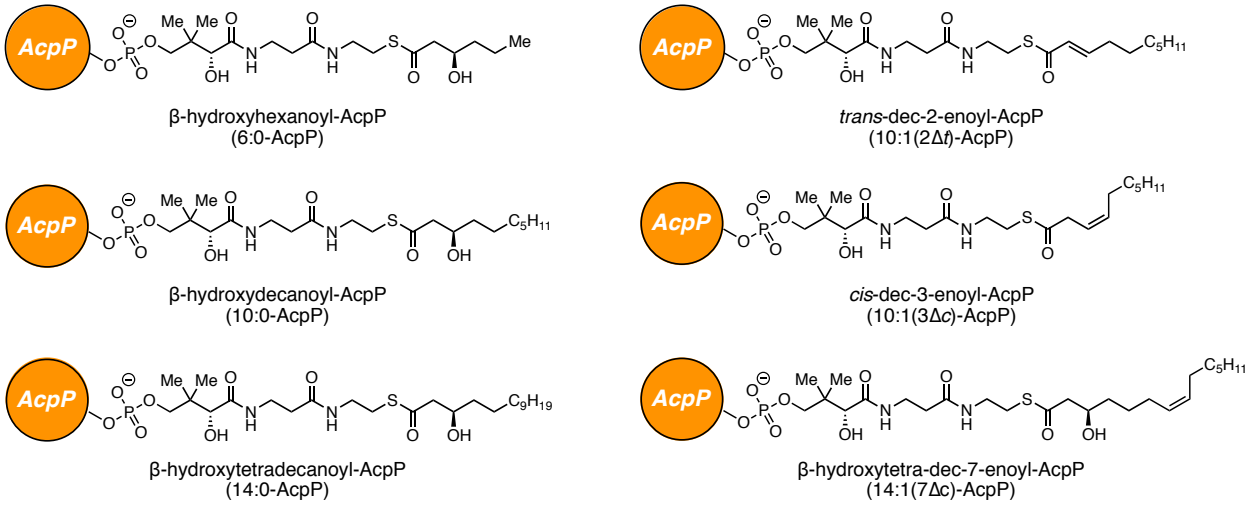

Figure S7. Acyl-AcpP substrates used in simulations of the acyl-AcpP$_2$•FabA$_2$ and acyl-AcpP$_2$•FabZ$_2$ complexes.

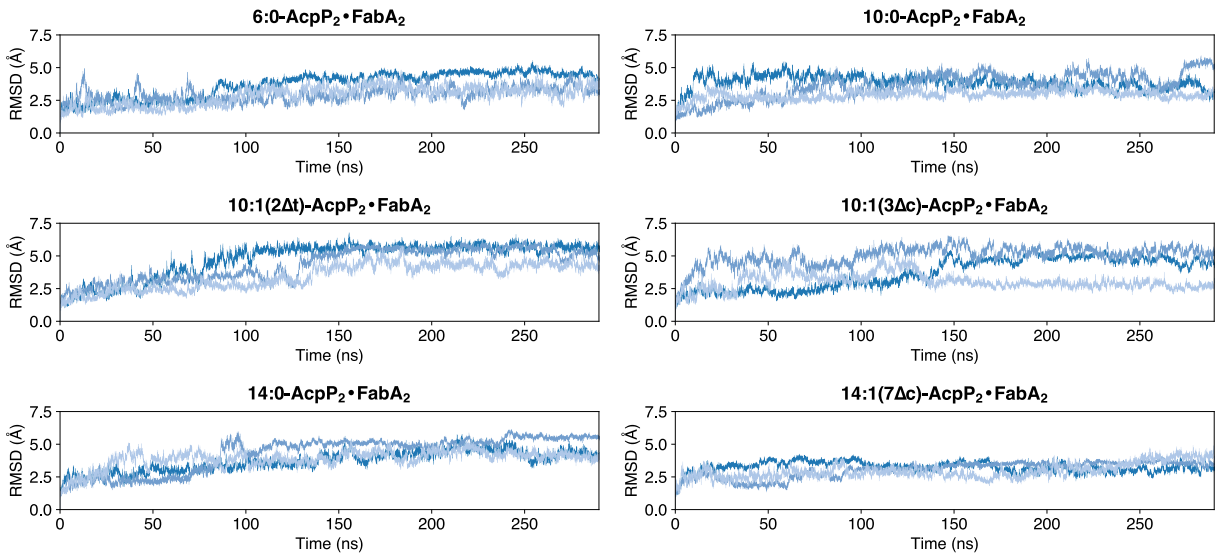

Figure S8. **Root mean square deviations (RMSDs) of acyl-AcpP$_2$•FabA$_2$ complexes observed during GaMD simulations**. The dark, medium and light blue curves represent independent 290ns simulations. To compute these RMSDs of each complex, every 10th snapshot of the coordinate data were extracted from the complete data set and superimposed using the C$_\alpha$s of the entire complex.

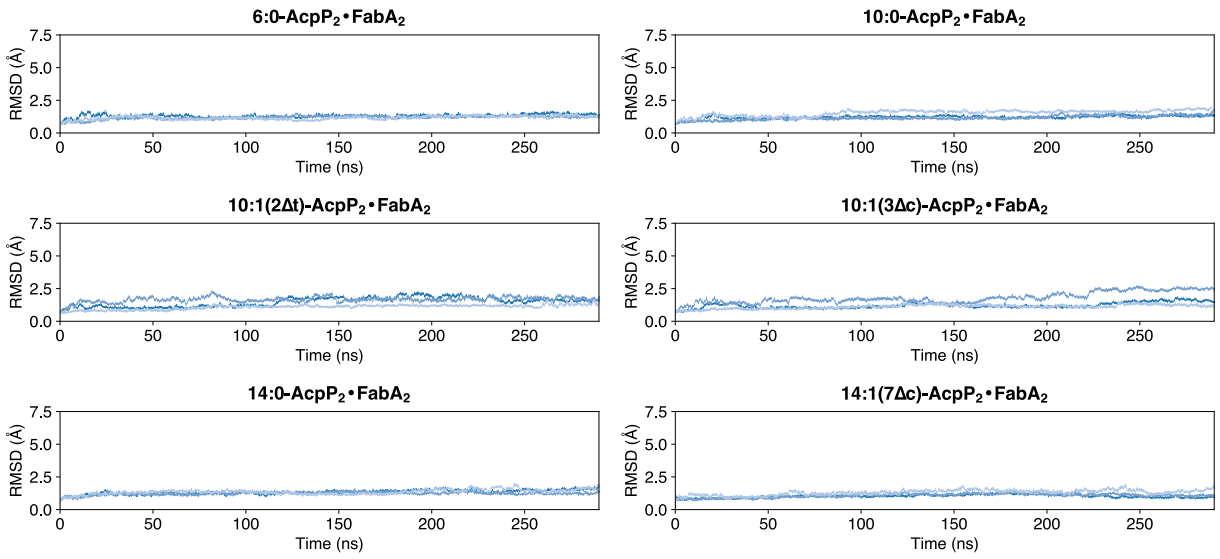

Figure S9. **RMSDs of the dimeric dehydratase subunit of acyl-AcpP$_2$•FabA$_2$ complexes observed during GaMD simulations**. The dark, medium and light blue curves represent data from an independent 290 ns simulation. Plots were generated by taking every 10th snapshot of the simulation data. To compute these RMSDs, in each case every 10th snapshot of the coordinate data were extracted from the complete data set and superimposed using the C$_\alpha$s of both dehydratases.

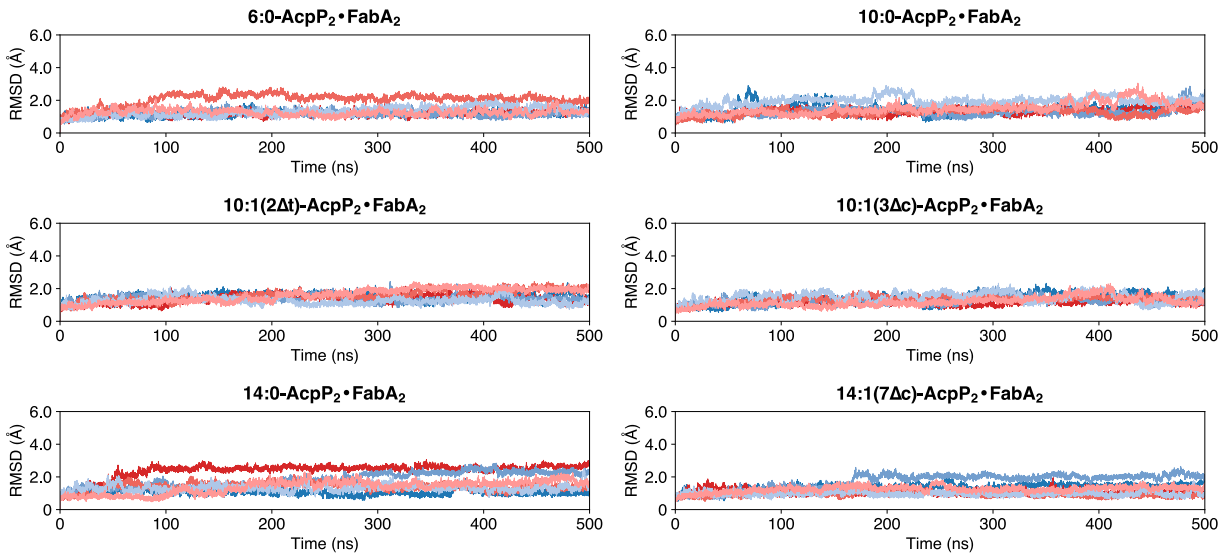

Figure S10. **RMSDs of AcpPs of acyl-AcpP$_2$•FabA$_2$ complexes observed during GaMD simulations**. Each blue (AcpP$_1$) and red (AcpP$_2$) curve represents data from an independent 290-ns. Plots were generated by taking every 10th snapshot of the simulation data. To compute these RMSDs, in each case every 10th snapshot of the coordinate data were extracted from the complete data set and superimposed using the C$_\alpha$s of both dehydratases so as to capture not only the internal motions of the carrier proteins but also their rotations and translations with respect to the dehydratases.

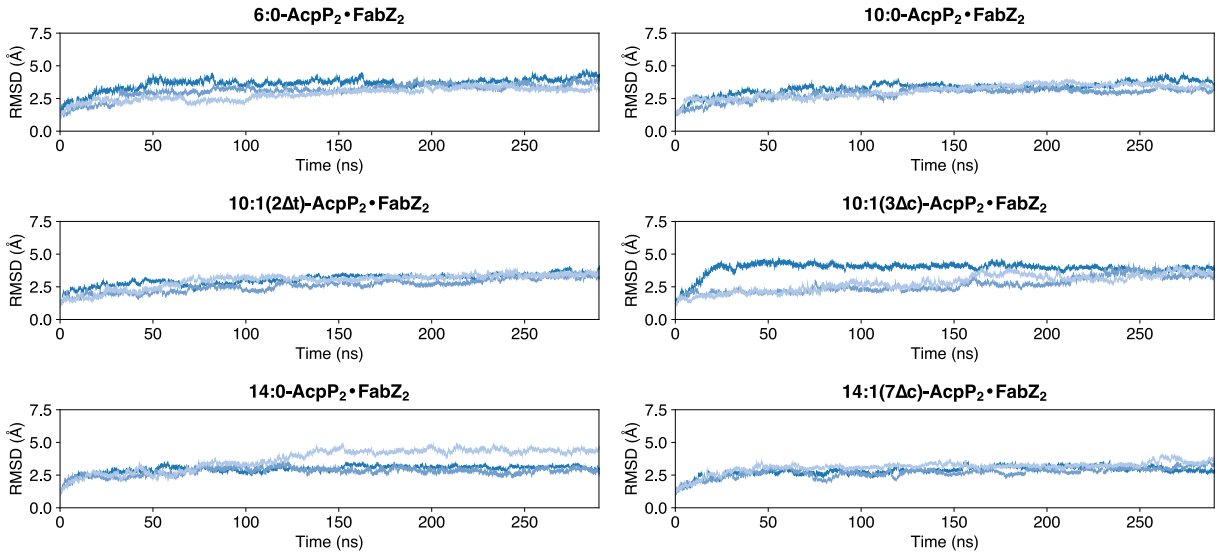

Figure S11. RMSDs of acyl-AcpP•FabZ$_2$ complexes observed during GaMD simulations. The dark, medium and light blue curves represent data from an independent 290-ns simulation. To compute these RMSDs of each complex, every 10th snapshot of the coordinate data were extracted from the complete data set and superimposed using the C_αs of the entire complex.

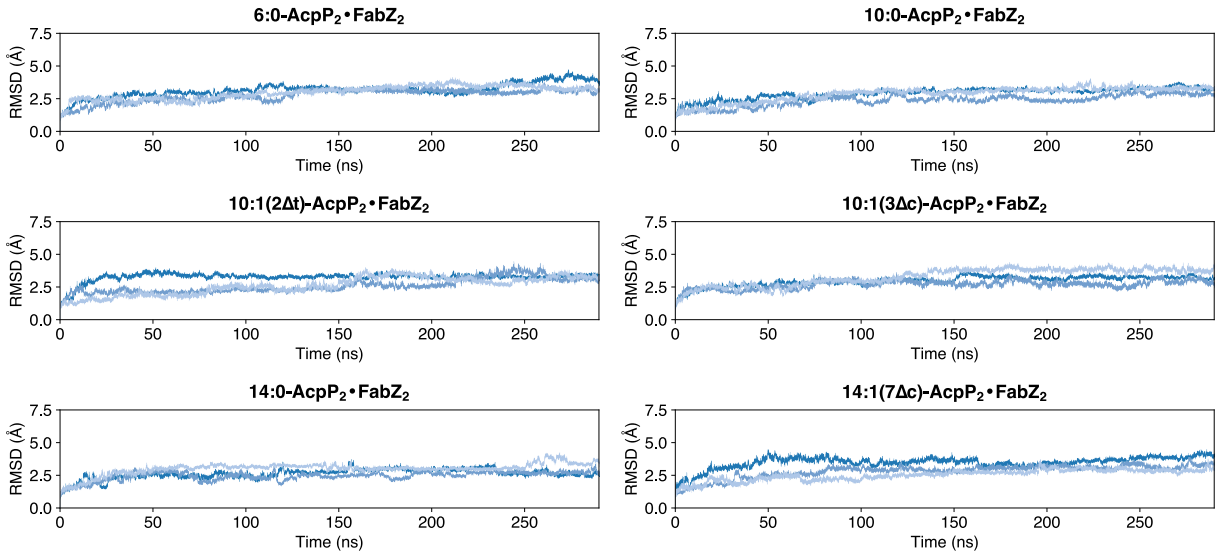

Figure S12. **RMSDs of dimeric dehydratase subunit of acyl-AcpP$_2$•FabZ$_2$ complexes observed during GaMD simulations**. The dark, medium and light blue curves represent data from an independent 290 ns simulation. Plots were generated by taking every 10th snapshot of the simulation data. To compute these RMSDs, in each case every 10th snapshot of the coordinate data were extracted from the complete data set and superimposed using the C$_\alpha$s of both dehydratases.

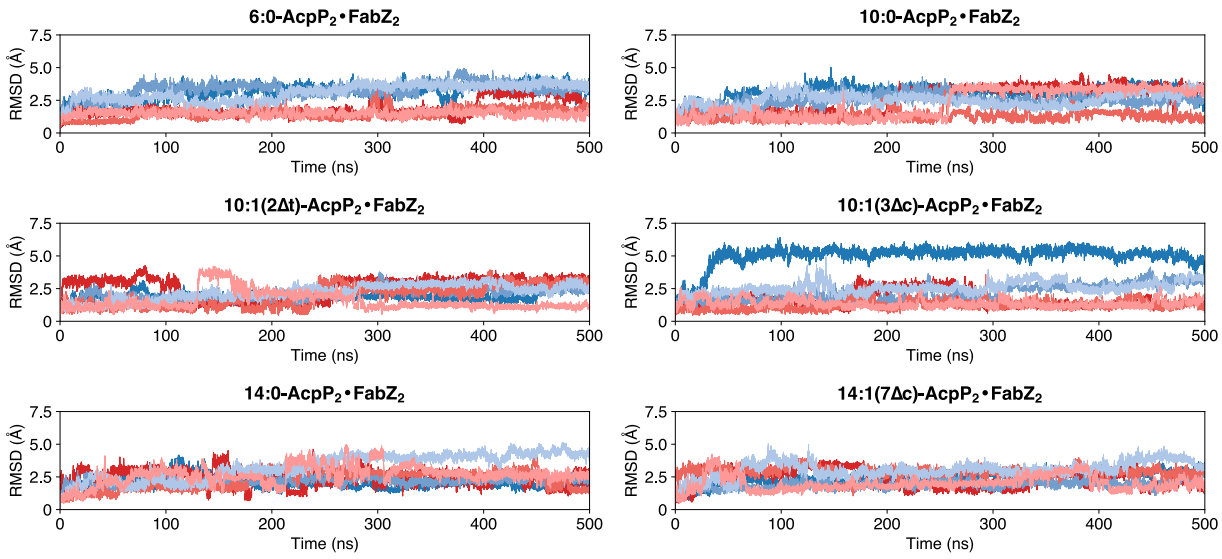

Figure S13. **RMSDs of AcpPs of acyl-AcpP$_2$•FabZ$_2$ complexes sampled during GaMD simulations**. Each blue (AcpP$_1$) and red (AcpP$_2$) curve represents data from an independent 290 ns simulation. To compute these RMSDs, in each case every 10th snapshot of the coordinate data were extracted from the complete data set and superimposed using the C$_\alpha$s of both dehydratases so as to capture not only the internal motions of the carrier proteins but also their rotations and translations with respect to the dehydratases.

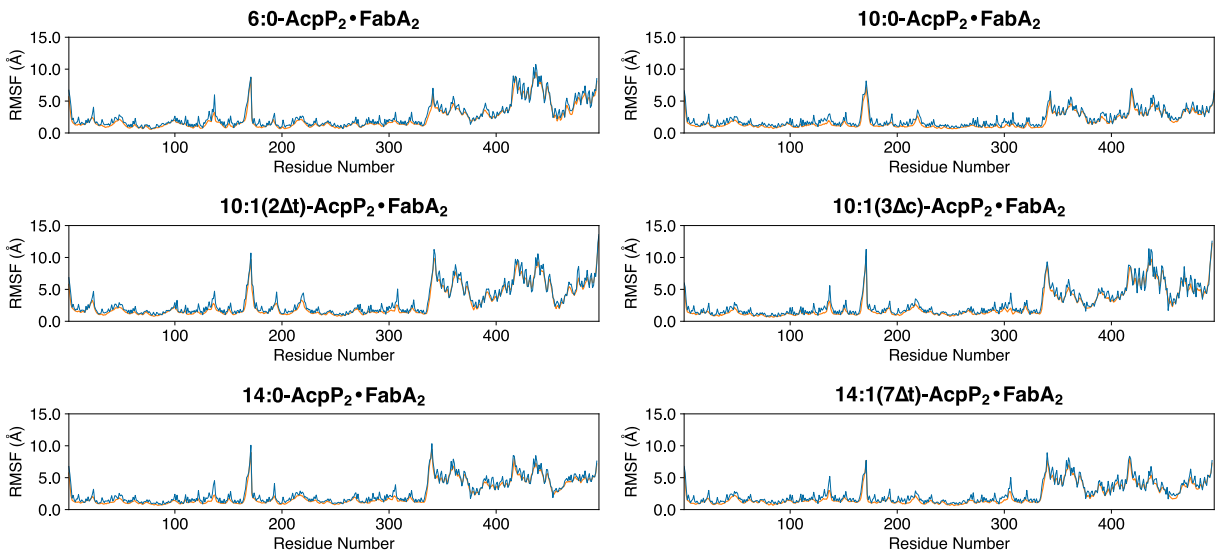

Figure S14. **Root mean square (RMS) fluctuations each residue of the acyl-AcpP$_2$•FabA$_2$ complexes subjected to GaMD simulations**. The blue curve shows the RMS fluctuations of the backbone – measured using backbone heavy (non-hydrogenic) atoms – of each residue, whereas the orange curve shows the RMS fluctuation of sidechains measured using each residue's sidechain heavy (non-hydrogen) atoms. Residue numbers indicate FabA monomer 1 (1-171), FabA monomer 2 (172-342), AcpP$_1$ (343-419) and AcpP$_2$ (420-496).

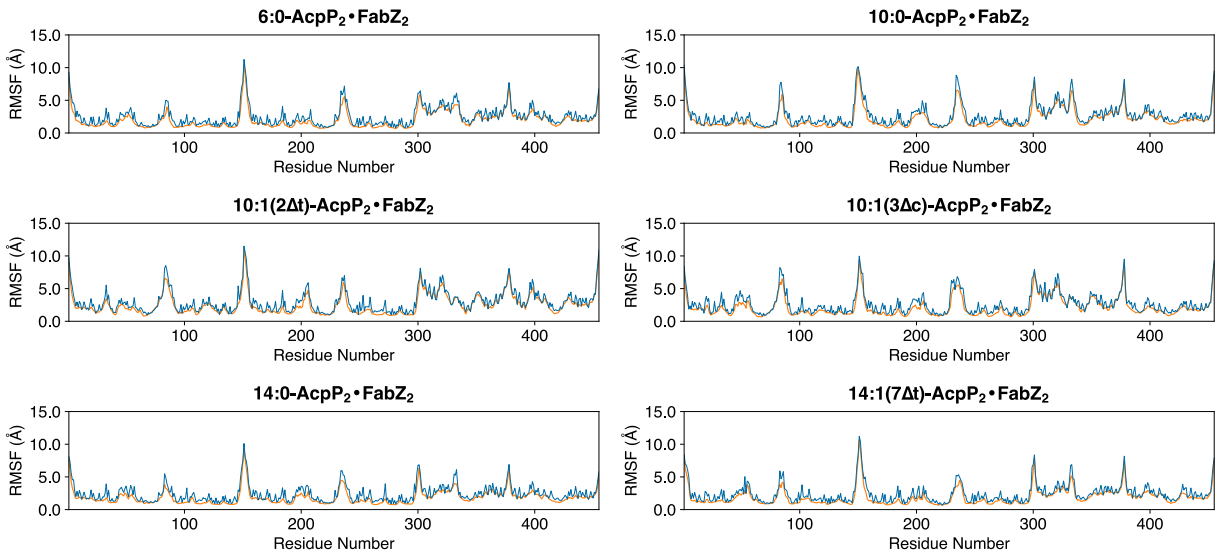

Figure S15. **RMS fluctuations each residue of the acyl-AcpP$_2$•FabZ$_2$ complexes subjected to GaMD simulations**. The blue curve shows the RMS fluctuations of the backbone – measured using backbone heavy (non-hydrogen) atoms – of each residue, whereas the orange curve shows the RMS fluctuation of side chains measured using each residue's side chain heavy (non-hydrogen) atoms. Residue numbers indicate FabZ monomer 1 (1-150), FabZ monomer 2 (151-301), AcpP$_1$ (302-378) and AcpP$_2$ (378-455).

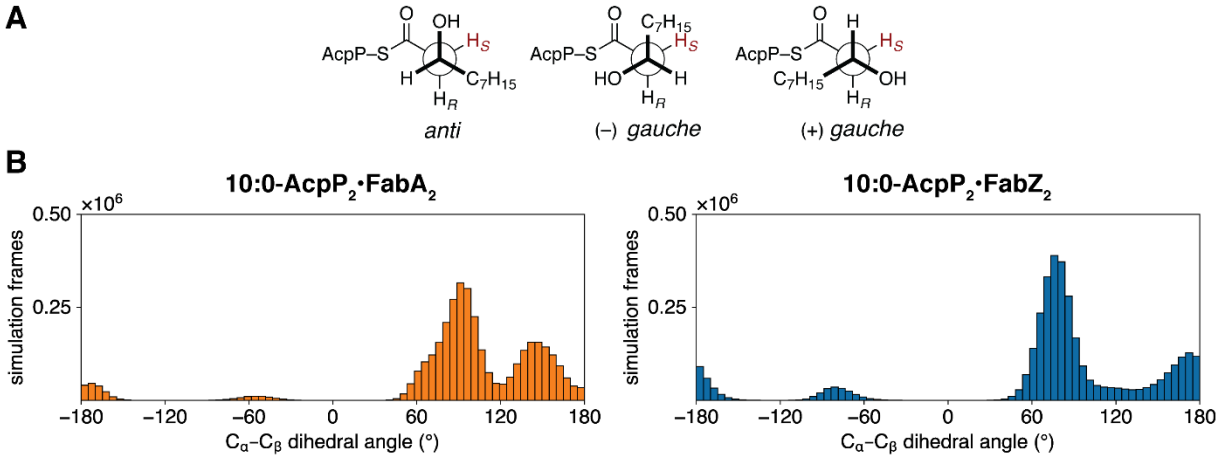

Figure S16. Distribution of dihedral angles for the C(O)–C_α–C_β–C_γ torsion sampled throughout the course of GaMD simulations of β-hydroxydecanoyl-AcpP•DHs. *A.*) Newman projections along the C_α–C_β bond of the (+) gauche (+60°), anti (180°), and (–) gauche (–60°) substrate rotamers of β-hydroxydecanoyl–AcpP. *B.*) Histograms of the C(O)–C_α–C_β–C_γ dihedral of the β-hydroxydecanoyl-AcpP sampled within the active sites of FabA (left-hand panel, orange bars) and FabZ (right-hand panel, blue bars). Simulation data were written every 0.5 ps and sorted into bins with width of 5°.

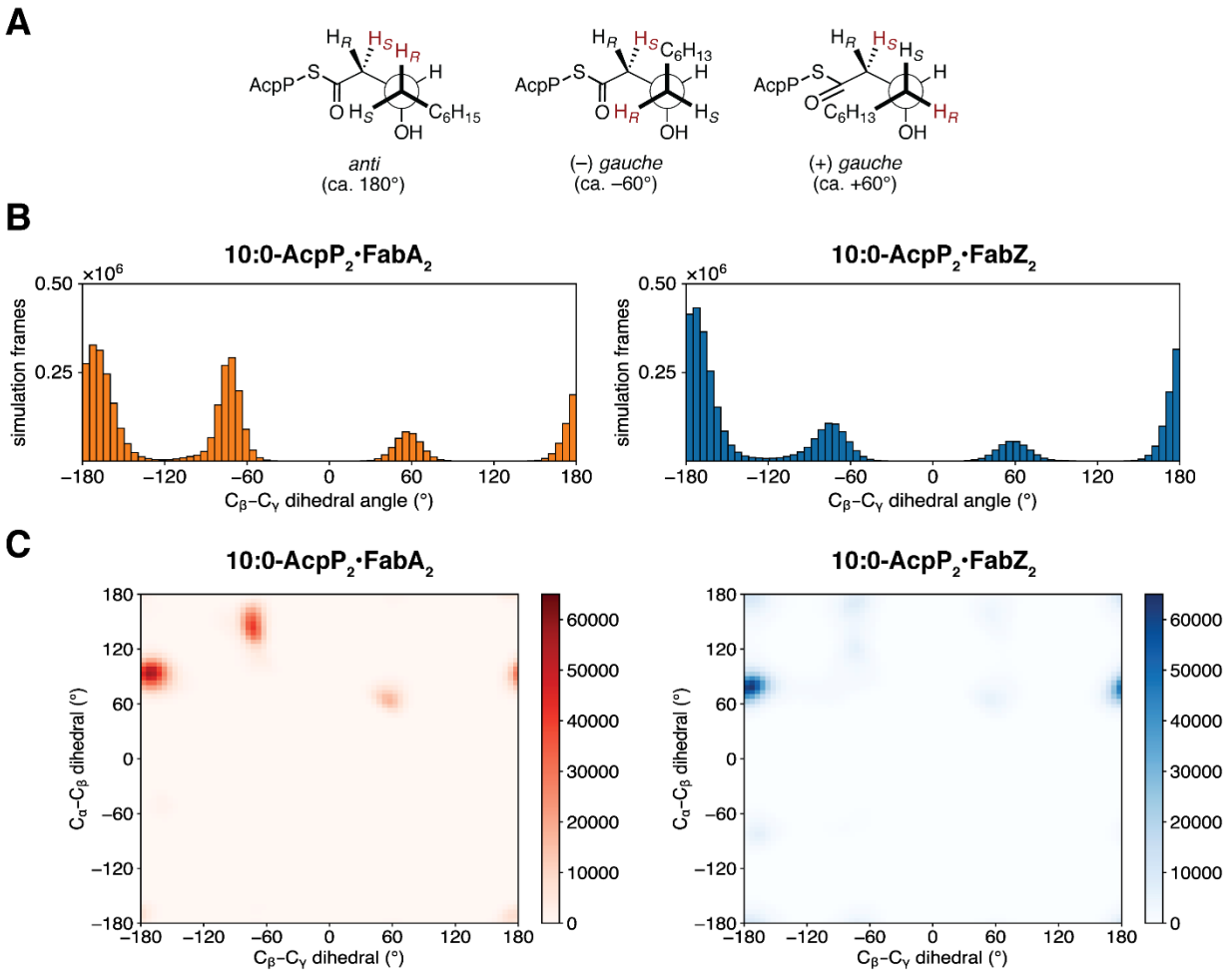

Figure S17. Distribution of dihedral angles for the C_α–C_β–C_γ–C_γ torsion sampled throughout the course of GaMD simulations of the β-hydroxydecanoyl-AcpP•DH complexes. *A.*) Newman projections of the C_β–C_γ bond of the (+) gauche (+60°), anti (180°), and (–) gauche (–60°) substrate rotamers of β-hydroxydecanoyl–AcpP. *B.*) Histograms of the C_α–C_β–C_γ–C_δ dihedral of the β-hydroxydecanoyl-AcpP sampled within the active sites of FabA (left-hand panel, orange bars) and FabZ (right-hand panel, blue bars). Simulation data were written every 0.5 ps and sorted into bins with width of 5°. *C.* 2D histogram of simulation data. Data were binned along two coordinates, the C(O)–C_α–C_β–C_γ and C_α–C_β–C_γ–C_δ torsion of the substrate. Data were sorted into 5° × 5° bins. Color bars indicate the absolute population of each histogram bin. Analysis of GaMD simulation data indicate FabA may preorganize its substrate for *trans* to *cis* isomerization before dehydration occurs. The 1D histograms (shown above) show that the (–) *gauche* conformation about the C_β–C_γ bond of the β-hydroxydecanoyl substrate is sampled to greater extent in the active site of FabA relative to that of FabZ. Note the (–) *gauche* arrangement of C_β–C_γ positions the pro-R H_γ close to the catalytic residues. The preferred C_α–C_β rotamer is (+) *gauche* conformation. Due to pentane interference, the substrate cannot – as illustrated in the 2D histograms shown above – adopt a C_α–C_β (+) *gauche*, C_β–C_γ (–) *gauche* conformation, which suggests a more complex mechanism for the FabA-catalyzed reaction than has been proposed in the literature. One intriguing possibility is that both the (+) *gauche* and *anti* C_α–C_β rotamers undergo (E1cb-like) dehydration, but only the *anti* conformer, in which the C_β–C_γ dihedral angle adopts the –60° value "required" for isomerization, is capable – upon dehydration – of undergoing further reaction to produce *cis*-dec-3-enoyl-AcpP.

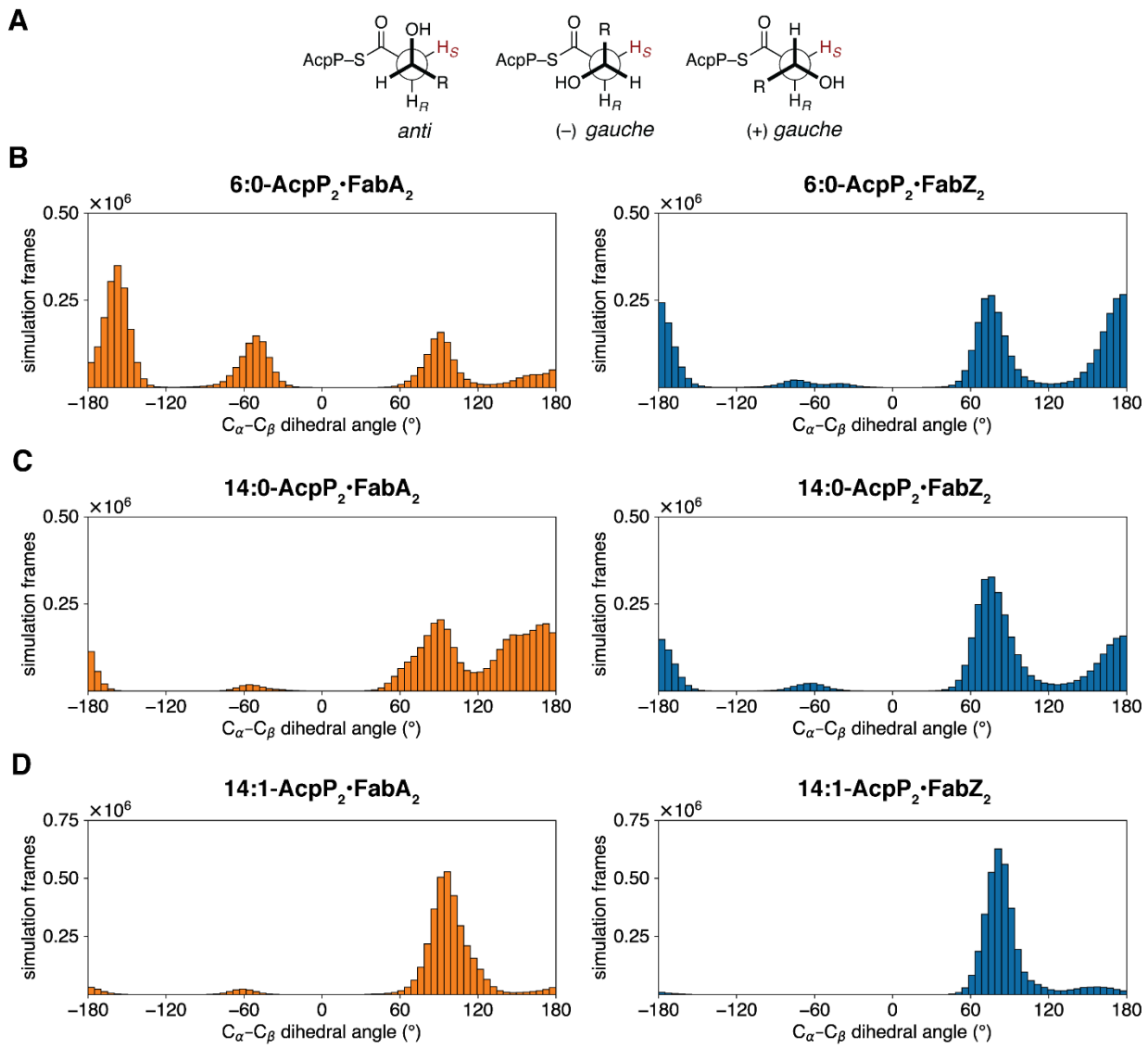

Figure S18. Distribution of dihedral angles for the substrate C(O)–C_α–C_β–C_γ torsion sampled throughout the course of GaMD simulations of β-hydroxyhexanoyl-AcpP•DHs, β-hydroxytetradecanoyl-AcpP•DHs and **β-hydroxytetradec-7-enoyl-AcpP•DHs**. *A.*) Newman projections along the C_α–C_β bond of the (+) gauche (+60°), anti (180°), and (–) gauche (–60°) substrate rotamers of β-hydroxyacyl-AcpP. *B-D.*) Histograms of the C(O)–C_α–C_β–C_γ dihedral of the β-hydroxyacyl-AcpP sampled within the active sites of FabA (left-hand panel, orange bars) and FabZ (right-hand panel, blue bars). Simulation data were written every 0.5 ps and sorted into bins with width of 5°. Analysis of conformational preferences of the β-hydroxyhexanoyl-AcpP (*B*), β-hydroxytetradecanoyl-AcpP (*C*), and β-hydroxytetradec-7-enoyl-AcpP (*D*) within the substrate binding pockets of FabA and FabZ are consistent with those of β-hydroxydecanoyl-AcpP (Figure S15) in that a (+) *gauche*-like conformation is sampled. Interestingly – in agreement with substrate preferences observed experimentally – this (reactive) *gauche*-like rotamer of β-hydroxyacyl-AcpP is sampled more frequently within the active site of FabZ than in the FabA pocket. Furthermore, rotation about this dihedral in longer chain substrates, in particular the β-hydroxytetradec-7-enoyl-AcpP, is much more hindered, likely to due to the additional steric bulk of these substrates.

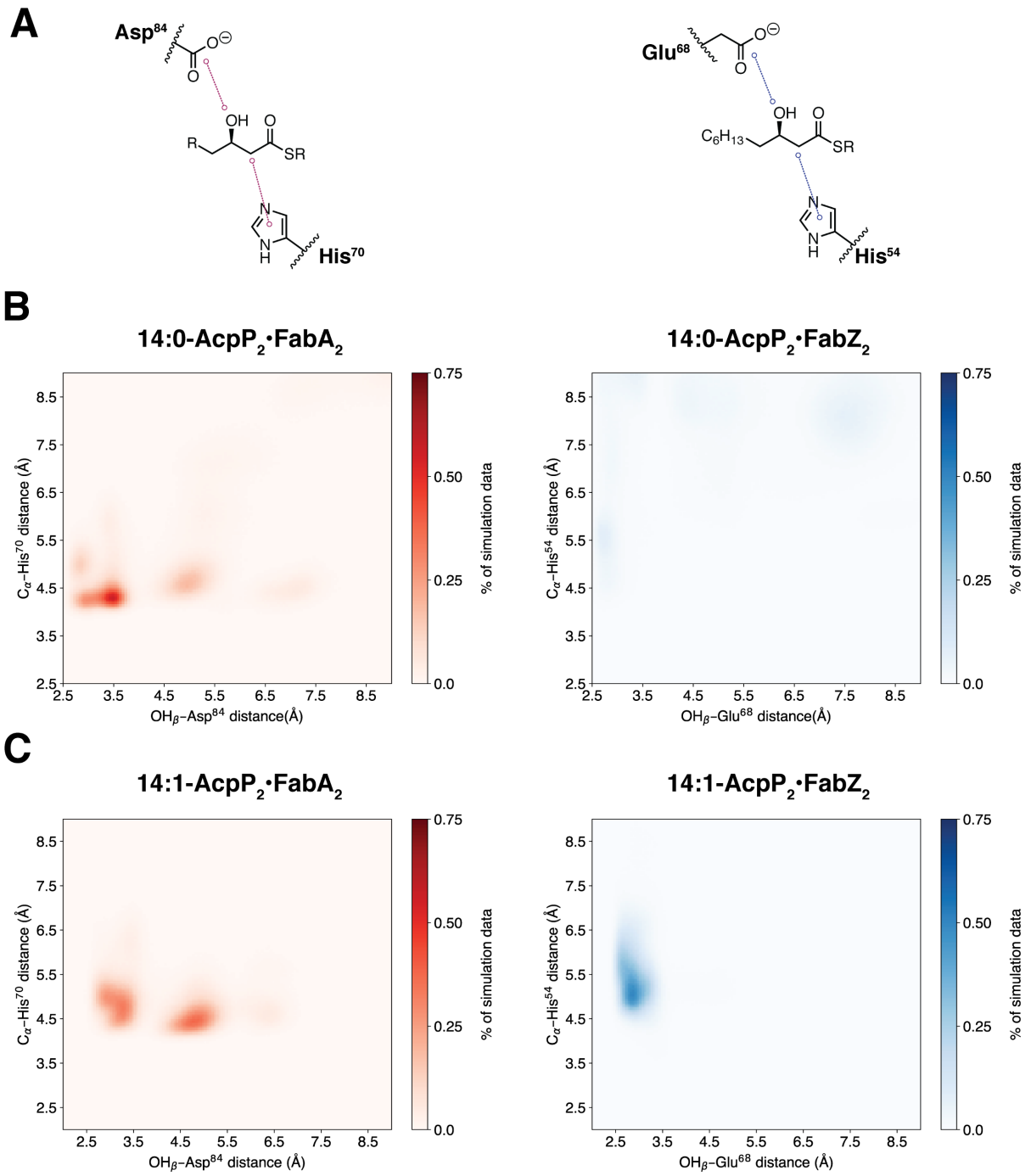

Figure S19. Distances between catalytic residues and key substrate moieties sampled in MD simulations of β-hydroxytetradecanoyl-AcpP•DHs and β-hydroxytetradec-7-enoyl-AcpP•DHs. 2D histogram of simulation data of the complexes of β-hydroxytetradecanoyl-AcpP•DHs and β-hydroxytetradec-7-enoyl-AcpP•DHs. Simulation data were binned along two coordinates (dimensions): the distance between the β-hydroxy oxygen of the substrate and the side chain carboxylate of FabA Asp^{84} or FabZ Glu^{68} (horizontal axis), and the distance between the imidazole of the catalytic histidine and the substrate α carbon (vertical axis). A. Illustrations of coordinates analyzed. B) Data from simulations of β-hydroxytetradecanoyl-Acp•FabA (left) and β-hydroxytetradecanoyl-Acp•FabZ (right). C) Data from simulations of β-hydroxytetradec-7-enoyl-AcpP•FabA (left) and β-hydroxytetradec-7-enoyl-AcpP•FabZ

(right). Data were sorted into 0.05 Å × 0.05 Å bins. Color bars indicate the absolute population of each histogram bin. Rock et al. have demonstrated that while both FabA and FabZ have low and similar activity towards β-hydroxytetradecanoyl-AcpP, β-hydroxytetradec-7-enoyl-AcpP undergoes reaction with FabZ with a 27-fold preference over FabA. [38] Comparison of the key distances between the substrate catalytic His and Asp (or Glu) of FabA (or FabZ) suggests an explanation for the observed selectivity. Namely, the FabZ's Glu^{68} is much more effective at maintaining a hydrogen bond with the β-hydroxy substituent of β-hydroxytetradec-7-enoyl-AcpP. In contrast, it is not clear based upon this analysis why β-hydroxytetradecanoyl-AcpP is similarly reactive with FabA and FabZ.

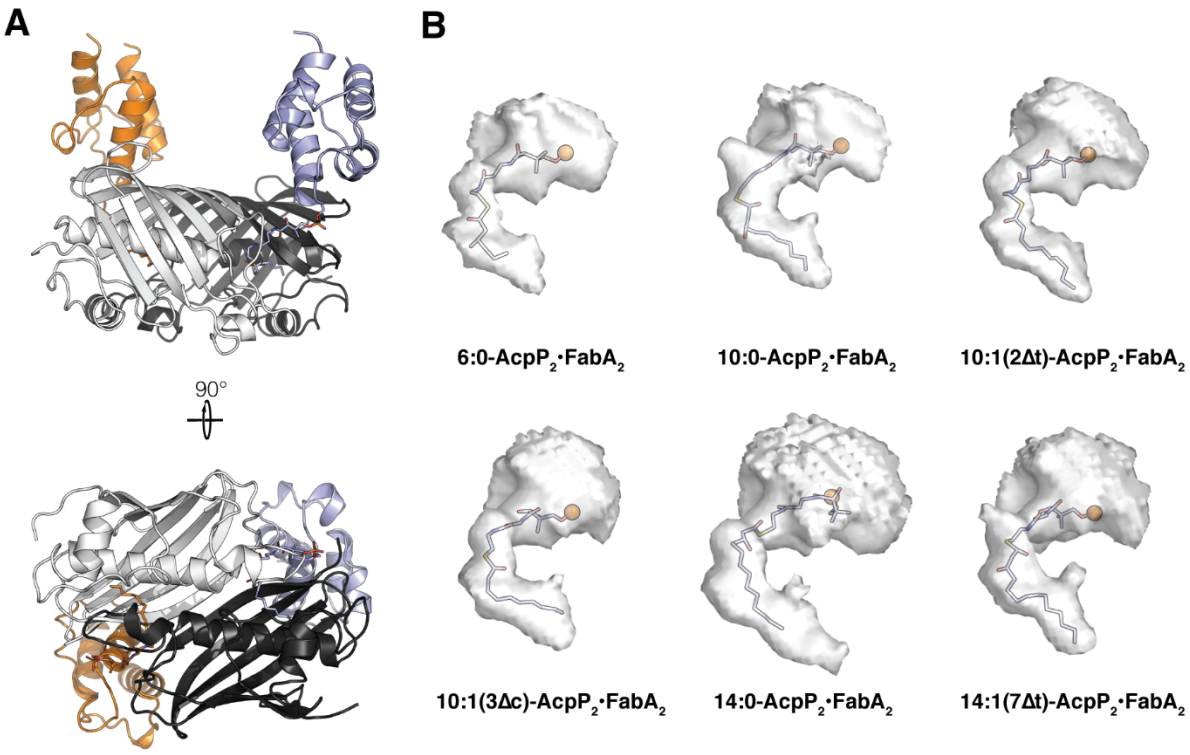

Figure S20. Cavities of the "first" active site of all acyl-AcpP$_2$•FabA$_2$ complexes sampled computationally. (*A*) Cartoon representation of the AcpP=FabA dimer. Rotation of the top view counterclockwise by 90° about the horizontal orients the complex in a suitable manner (bottom image) for visualization of the acyl substrate chain within the FabA active site. (*B*) Isosurfaces of the acyl-AcpP•FabA complexes sampled via MD simulation. 90% simulation data of each of these complexes possess an active site cavity that assumes a volume located within the rendered isosurface. The phosphantethiene prosthetic group and acyl substrate are shown as sticks. The phosphorus atom of phosphantiethiene is shown as an orange sphere. Note that the computed cavities include unoccupied space (upper regions of isosurfaces) between the carrer protein and the dehydratase (i.e, AcpP•DH interface).

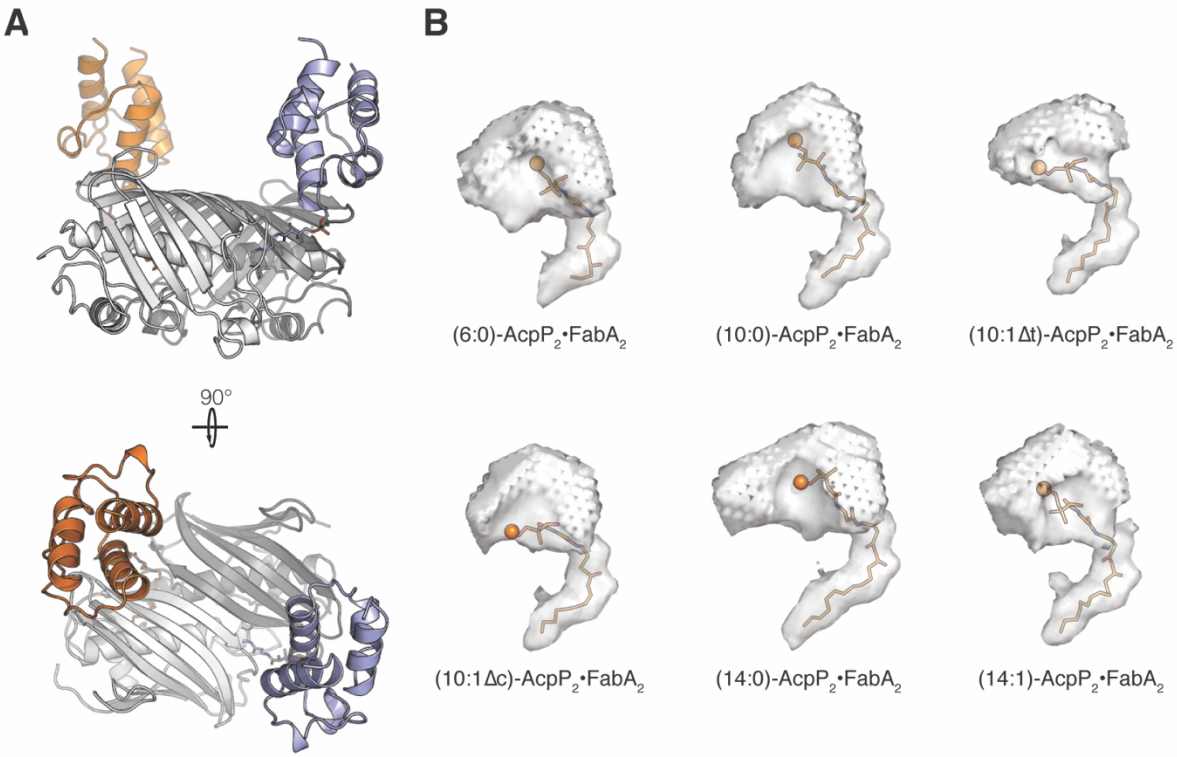

Figure S21. Cavities of the "second" active site of all acyl-AcpP$_2$•FabA$_2$ complexes sampled computationally . (*A*) Cartoon representation of the AcpP=FabA dimer. Rotation of the top view clockwise by 90° about the horizontal orients the complex in a suitable manner (bottom image) for visualization of the acyl substrate chain within the FabA active site. (*B*) Isosurfaces of the acyl-AcpP•FabA complexes sampled via MD simulation. 90% simulation data of each of these complexes possess an active site cavity that assumes a volume located within the rendered isosurface. The phosphantethiene prosthetic group and acyl substrate are shown as sticks. The phosphorus atom of phosphantiethiene is shown as an orange sphere. Note that the computed cavities include unoccupied space (upper regions of isosurfaces) between the carrer protein and the dehydratase (i.e, AcpP•DH interface).

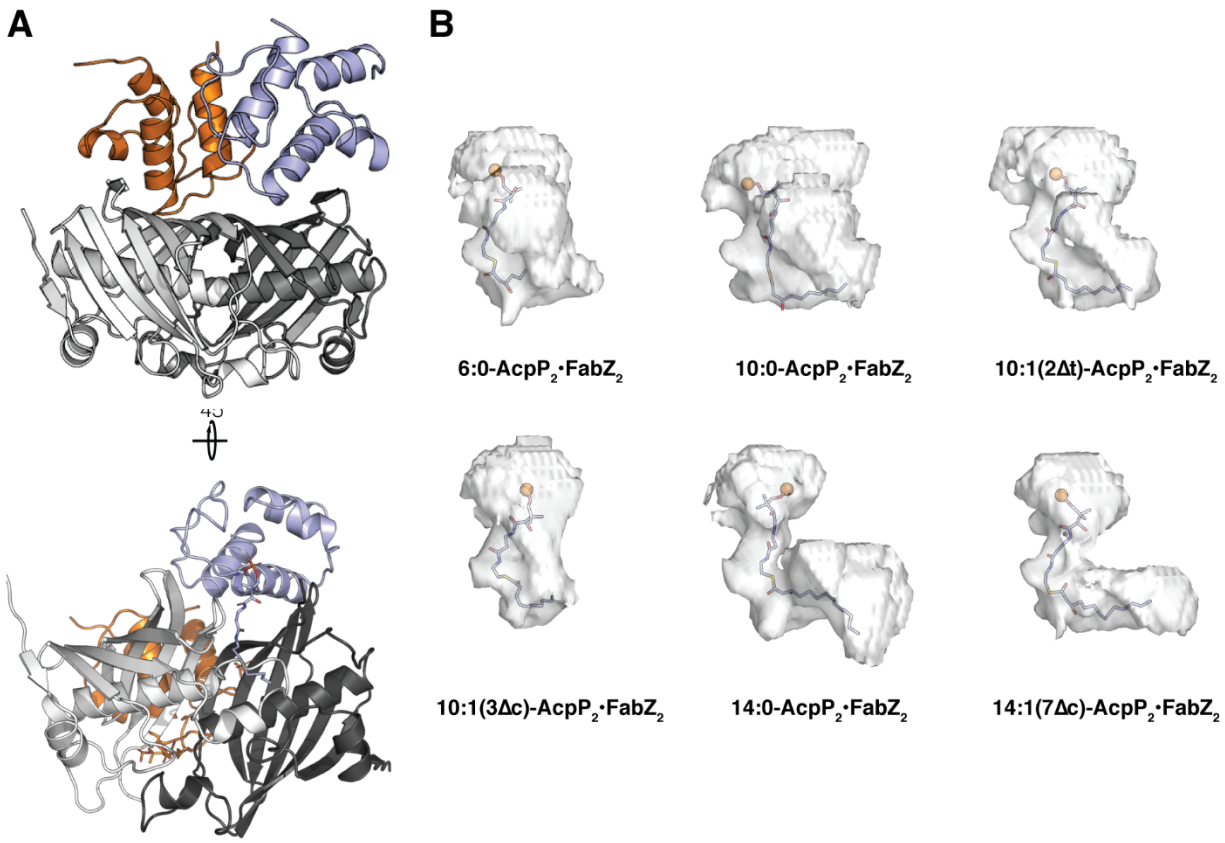

Figure S22. Cavities of the "first" active site of all acyl-AcpP$_2$•FabZ$_2$ complexes sampled computationally. (*A*) Cartoon representation of the AcpP=FabZ dimer oriented in a suitable manner (bottom image) for the visualization of the acyl substrate chain within the FabZ active site. (*B*) Isosurfaces of the acyl-AcpP•FabZ complexes sampled via MD simulation. 90% simulation data of each of these complexes possess an active site cavity within the rendered isosurface. The phosphantethiene prosthetic group and acyl substrate are shown as sticks. The phosphorus atom of phosphantiethiene is shown as an orange sphere. Note that the computed cavities include unoccupied space (upper regions of isosurfaces) between the carrer protein and the dehydratase. (i.e, AcpP•DH interface).

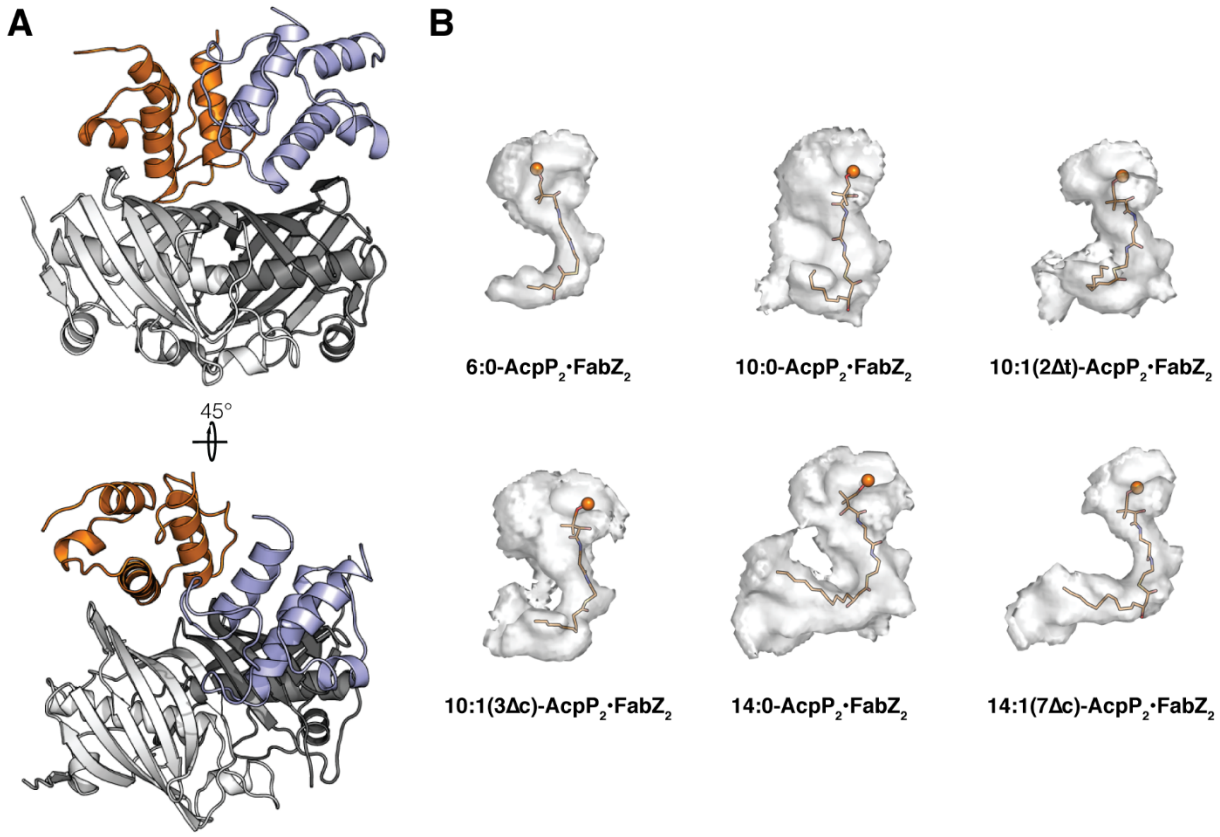

Figure S23. Cavities of the "second" active site of all acyl-AcpP$_2$•FabA$_2$ complexes sampled computationally . (*A*) Cartoon representation of the AcpP=FabZ dimer oriented in a suitable manner (bottom image) for the visualization of the acyl substrate chain within the FabZ active site. (*B*) Isosurfaces of the acyl-AcpP•FabZ complexes sampled via MD simulation. 90% simulation data of each of these complexes possess an active site cavity within the rendered isosurface. The phosphantethiene prosthetic group and acyl substrate are shown as sticks. The phosphorus atom of phosphantiethiene is shown as an orange sphere. Note that the computed cavities include unoccupied space (upper regions of isosurfaces) between the carrer protein and the dehydratase. (i.e, AcpP•DH interface).

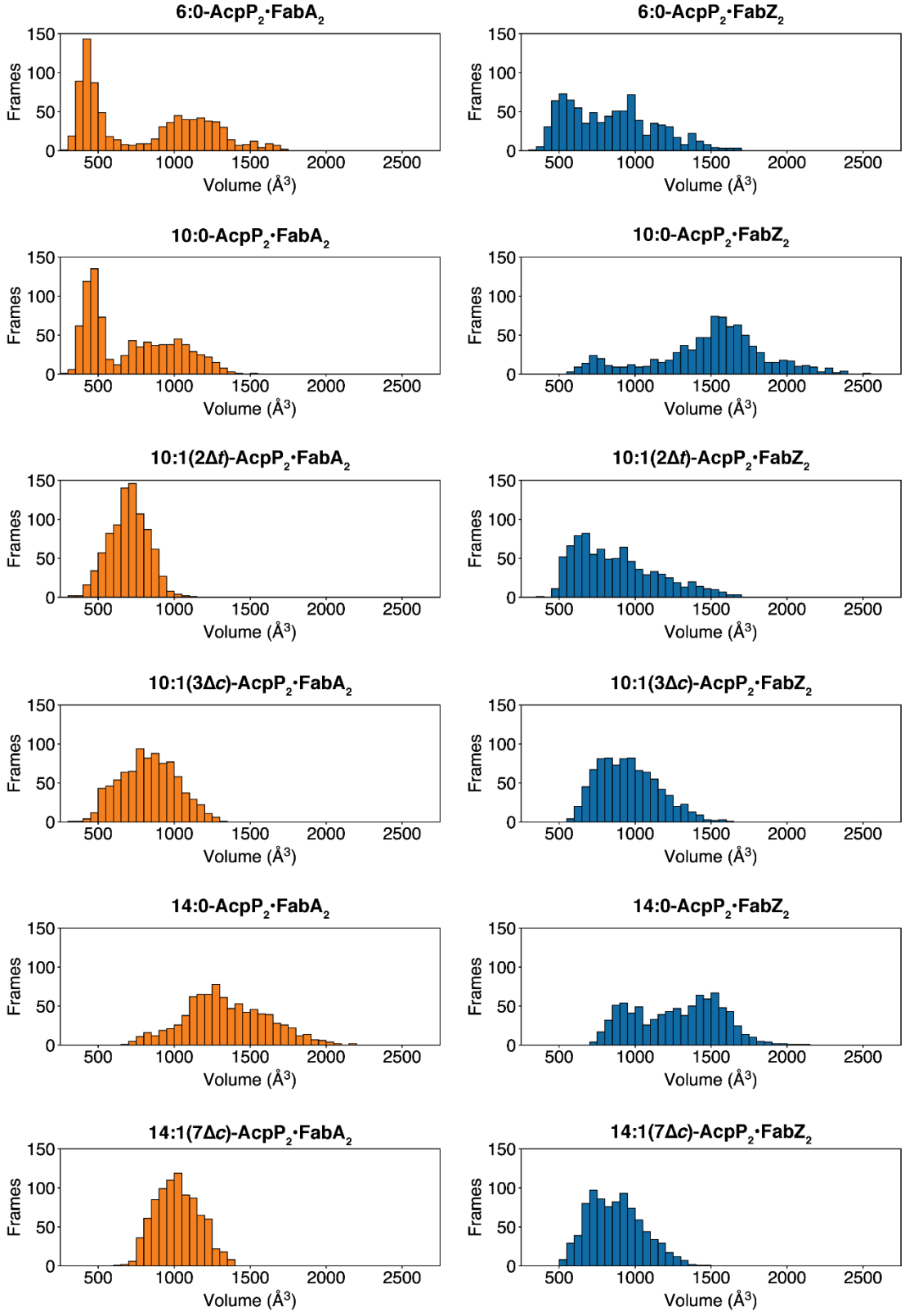

Figure S24. Distribution of substrate binding cavity volumes sample during the course of GaMD simulations of acyl-AcpP•FabA and acyl-AcpP•FabZ determined using POVME. Note that these

distrubutions were generated using a subset of the entire simulation data consisting of 435 simulation frames.

Table S1 Turbidity of Mocr-FabZ after TEV protease cleavage.

	Mocr-FabZ*	+ 25 μM *apo*-AcpP	+ 50 μM *apo*-AcpP	+ 150 μM *apo*-AcpP	+ 300 μM *apo*-AcpP	+ 500 μM *apo*-AcpP
OD_{600}	0.07 ± 0.02	0.04 ± 0.01	0.03 ± 0.01	0.01 ± 0.01	0.01 ± 0.01	0.01 ± 0.01

*Cleavage reactions were done in reaction mixes with 50 μM Mocr-FabZ subunit.

Table S2. Crystallographic summary.

Diffraction data	***AcpP=FabZ***
Space group	$P2_12_12_1$
Unit cell a, b, c (Å)	65.1, 136.2, 152.2
Wavelength (Å)	1.033
d_{min} *(Å)*	2.5 (2.59 – 2.50)*
Observations (#)	307,308 (29,936)
Unique reflections (#)	47,665 (4,689)
Mean I/σ_I	10.22 (1.12)
R_{merge}	0.150 (1.634)
$CC_{1/2}$	0.99 (0.479)
*CC**	0.99 (0.805)
Completeness (%)	0.99 (0.99)
Wilson B (Å²)	66.9
Refinement	
Reflections (#)	47,645
R_{work}	0.208
R_{free}	0.253
RMSD bonds (Å)	0.009
RMSD angles (°)	1.27
Atoms (#)	
Protein	10,369
Solvent	58
DH6 Probe	348
Average B-factors (Å²)	
Protein	84.2
Solvent	64.3
DH6 Probe	82.2
Ramachandran	
Favored (%)	94.7
Allowed (%)	5.1
Outliers (%)	0.2
# of TLS groups	82

* Values in parentheses refer to the outermost shell of data.

Table S3. Comparison of AcpP•DH interfacial contacts.

AcpP amino acids

AcpP Binding Partner	*Acidic residues*	*Basic residues*	*Hydrophobic residues*	*Hydrophilic residues*
AcpP=FabZ	E41, E47, E48, D56, D35	N/A	L37, V40, M44	S36
AcpP=FabA (4KEH)	E41, E47, E53, D56, E60	N/A	L37, V40, M44	S36

DH amino acids

AcpP Binding Partner	*Non-Crosslinked Subunit: Basic residues*	*Non-Crosslinked Subunit: Hydrophobic residues*	*Non-Crosslinked Subunit: Hydrophilic residues*	*Crosslinked Subunit: Basic residues*
AcpP=FabZ	K119, R121, R122, R126	L124, M144	D97	R100, K102
AcpP=FabA (4KEH)	R132, R136, R137, K161	L106, V134, L138, M140	N135	N/A

Table S4. Primers used for Cloning

Primer	Primer Sequence (5' to 3')
fabz fwd LIC	*TACTTCCAATCCAATGCNACCACCAATACCCATACCTTACAGATTG*
fabz rev LIC	*TTATCCACTTCCAATGTTATTATCCACTTCCAATGTTA*

D. Additional References

1. Yu X, Liu T, Zhu F, & Khosla C (2011) In vitro reconstitution and steady-state analysis of the fatty acid synthase from *Escherichia coli*. *Proc. Natl. Acad. Sci. USA* 108(46):18643-18648.

2. DelProposto J, Majmudar CY, Smith JL, & Brown WC (2009) Mocr: A novel fusion tag for enhancing solubility that is compatible with structural biology applications. *Protein Expression Purif.* 63(1):40-49.

3. Whicher JR*, et al.* (2013) Cyanobacterial polyketide synthase docking domains: a tool for engineering natural product biosynthesis. *Chem. Biol.* 20(11):1340-1351.

4. Eschenfeldt WH, Lucy S, Millard CS, Joachimiak A, & Mark ID (2009) A family of LIC vectors for high-throughput cloning and purification of proteins. *High Throughput Protein Expression and Purification*, (Springer), pp 105-115.

5. Kimber MS*, et al.* (2004) The structure of (3R)-hydroxyacyl-acyl carrier protein dehydratase (FabZ) from *Pseudomonas aeruginosa*. *J. Biol. Chem.* 279(50):52593-52602.

6. McCoy AJ*, et al.* (2007) Phaser crystallographic software. *J. Appl. Crystallogr.* 40(4):658-674.

7. Nguyen C*, et al.* (2014) Trapping the dynamic acyl carrier protein in fatty acid biosynthesis. *Nature* 505(7483):427-431.

8. Emsley P, Lohkamp B, Scott WG, & Cowtan K (2010) Features and development of Coot. *Acta Crystallogr. Sect. D. Biol. Crystallogr.* 66(4):486-501.

9. Adams PD*, et al.* (2010) PHENIX: A comprehensive Python-based system for macromolecular structure solution. *Acta Crystallogr. Sect. D. Biol. Crystallogr.* 66(2):213-221.

10. Chen VB*, et al.* (2010) MolProbity: All-atom structure validation for macromolecular crystallography. *Acta Crystallogr. Sect. D. Biol. Crystallogr.* 66(1):12-21.

11. Schrodinger, LLC (2015) The PyMOL Molecular Graphics System, Version 1.8.

12. Krissinel E & Henrick K (2007) Inference of Macromolecular Assemblies from Crystalline State. *J. Mol. Biol.* 372(3):774-797.

13. Cieplak P, Cornell WD, Bayly C, & Kollman PA (1995) Application of the multimolecule and multiconformational RESP methodology to biopolymers: Charge derivation for DNA, RNA, and proteins. *J. Comput. Chem.* 16(11):1357-1377.

14. Frisch MJ*, et al.* (2009) Gaussian 09 Revision D.01. *Gaussian, Inc. Wallingford CT*:2-3.

15. Maier JA*, et al.* (2015) ff14SB: Improving the Accuracy of Protein Side Chain and Backbone Parameters from ff99SB. *J. Chem. Theory Comput.* 11(8):3696-3713.

16. Wang J, Wolf RM, Caldwell JW, Kollman PA, & Case DA (2004) Development and testing of a general Amber force field. *J. Comput. Chem.* 25(9):1157-1174.

17. Bashford D & Karplus M (1990) pKa's of Ionizable Groups in Proteins: Atomic Detail from a Continuum Electrostatic Model. *Biochemistry* 29(44):10219-10225.

18. Gordon JC*, et al.* (2005) H++: A server for estimating pKas and adding missing hydrogens to macromolecules. *Nucleic Acids Res.* 33(SUPPL. 2):W368-W371.

19. Myers J, Grothaus G, Narayanan S, & Onufriev A (2006) A simple clustering algorithm can be accurate enough for use in calculations of pKs in macromolecules. *Proteins: Struct., Funct., Genet.* 63(4):928-938.

20. Anandakrishnan R, Aguilar B, & Onufriev AV (2012) H++ 3.0: Automating pK prediction and the preparation of biomolecular structures for atomistic molecular modeling and simulations. *Nucleic Acids Res.* 40(W1).

21. Jorgensen WL, Chandrasekhar J, Madura JD, Impey RW, & Klein ML (1983) Comparison of simple potential functions for simulating liquid water. *J. Chem. Phys.* 79(2):926-935.

22. Case DA*, et al.* (2014) AMBER14 (University of California, San Francisco).

23. Hamelberg D, Mongan J, & McCammon JA (2004) Accelerated molecular dynamics: A promising and efficient simulation method for biomolecules. *J. Chem. Phys.* 120(24):11919-11929.

24. Pierce LCT, Salomon-Ferrer R, Augusto F. De Oliveira C, McCammon JA, & Walker RC (2012) Routine access to millisecond time scale events with accelerated molecular dynamics. *J. Chem. Theory Comput.* 8(9):2997-3002.

25. Salomon-Ferrer R, Götz AW, Poole D, Le Grand S, & Walker RC (2013) Routine microsecond molecular dynamics simulations with AMBER on GPUs. 2. Explicit solvent particle mesh ewald. *J. Chem. Theory Comput.* 9(9):3878-3888.

26. Miao Y, Feher VA, & McCammon JA (2015) Gaussian Accelerated Molecular Dynamics: Unconstrained Enhanced Sampling and Free Energy Calculation. *J. Chem. Theory Comput.* 11(8):3584-3595.

27. Miao Y*, et al.* (2014) Improved reweighting of accelerated molecular dynamics simulations for free energy calculation. *J. Chem. Theory Comput.* 10(7):2677-2689.

28. Ryckaert JP, Ciccotti G, & Berendsen HJC (1977) Numerical integration of the cartesian equations of motion of a system with constraints: molecular dynamics of n-alkanes. *J. Comput. Phys.* 23(3):327-341.

29. Darden T, York D, & Pedersen L (1993) Particle mesh Ewald: An $N \cdot \log(N)$ method for Ewald sums in large systems. *J. Chem. Phys.* 98(12):10089-10092.

30. Loncharich RJ, Brooks BR, & Pastor RW (1992) Langevin dynamics of peptides: The frictional dependence of isomerization rates of N-acetylalanyl-N′-methylamide. *Biopolymers* 32(5):523-535.

31. Roe DR & Cheatham TE (2013) PTRAJ and CPPTRAJ: Software for processing and analysis of molecular dynamics trajectory data. *J. Chem. Theory Comput.* 9(7):3084-3095.

32. McGibbon RT*, et al.* (2015) MDTraj: A Modern Open Library for the Analysis of Molecular Dynamics Trajectories. *Biophys. J.* 109(8):1528-1532.

33. Dennington R, Keith T, & Millam J (2016) Gaussview, Version 5).

34. Hanwell MD*, et al.* (2012) Avogadro: An advanced semantic chemical editor, visualization, and analysis platform. *J. Cheminf.* 4(17).

35. Wagner JR*, et al.* (2017) POVME 3.0: software for mapping binding pocket flexibility. *J. Chem. Theory Comput.* 13(9):4584-4592.

36. Durrant JD, Votapka L, Sørensen J, & Amaro RE (2014) POVME 2.0: an enhanced tool for determining pocket shape and volume characteristics. *J. Chem. Theory Comput.* 10(11):5047-5056.

37. Durrant JD, de Oliveira CAF, & McCammon JA (2011) POVME: an algorithm for measuring binding-pocket volumes. *J. Mol. Graphics Model.* 29(5):773-776.

38. Heath RJ & Rock CO (1996) Roles of the FabA and FabZ β-hydroxyacyl-acyl carrier protein dehydratases in *Escherichia coli* fatty acid biosynthesis. *J. Biol. Chem.* 271(44):27795-27801.